EPJ Photovoltaics **16**, 11 (2025)

https://doi.org/10.1051/epjpv/2024045

Available online at:
www.epj-pv.org

ORIGINAL ARTICLE OPEN ACCESS

Contactless defects detection using modulated photoluminescence technique: model for a single Shockley-Read-Hall trap in a semiconductor thin layer

Baptiste Bérenguier[1,2,*], Alban Asseko[1,2], Hiba Haddara[1,2,3,4], Sylvain Le Gall[1,3,4], Jean-Paul Kleider[1,3,4], and Jean-François Guillemoles[1,2]

[1] Institut Photovoltaïque d'Ile de France (ITE), 18 Boulevard Thomas Gobert, 91120 Palaiseau, France
[2] Institut Photovoltaïque d'Ile de France (IPVF), UMR 9006, CNRS, Ecole Polytechnique, IP Paris, Chimie Paristech, PSL, 91120 Palaiseau, France
[3] Université Paris-Saclay, CentraleSupélec, CNRS, Laboratoire de Génie Electrique et Electronique de Paris, 91192 Gif-sur-Yvette, France
[4] Sorbonne Université, CNRS, Laboratoire de Génie Electrique et Electronique de Paris, 75252 Paris, France

Received: 24 July 2024 / Accepted: 25 November 2024

Abstract. Studying defects in semiconductors is, in practice, a very important topic for opto-electronic applications. It involves advanced characterization tools able to quantify and qualify the defect densities present in the materials. In the present article we focus on the use of a contactless frequency domain technique: modulated photoluminescence (MPL), and show its potential to detect defects. MPL has been used for the measurement of differential lifetime for several decades in silicon wafers. By extending it to low lifetime/highly defective materials we discovered its potential to become a defect spectroscopy method, measuring time constants close to the ones governing impedance spectroscopy measurements. Proofs of concept and an analytical model for doped materials have been presented already. Here, we reformulate the analytical model more explicitly and check its applicability by extensive numerical simulations for the case of a low illumination for a thin layer with a single defect. We present a parametric numerical study simulating the response of a single Shockley-Read-Hall center, showing the appearance of so-called V-Shapes in the MPL phase patterns as predicted by the analytical model, and valid beyond small-signal approximation. We discuss the difference between these two approaches and extend the analytical model and numerical investigations to intrinsic materials.

Keywords: Modulated photoluminescence / frequency domain technique / photocarrier radiometry / photovoltaic absorbers

1 Introduction

Probing the recombination inside a semiconductor layer or stack of layers is a mandatory task for the development of multi-layer devices such as solar cells, laser diodes, or any kind of mono-dimensional semiconductor architectures. Any semiconductor exhibits intrinsically radiative recombination and Auger recombination, but in many cases the device performance is limited by extrinsic recombination centers that can be generated by various types of defects like impurities, defaults in the crystalline network, dangling bonds at the surface or interfaces, etc. If the device presents a space charge layer (e.g. due to a pn or Schottky junction) and is fitted with electrical contacts, one can use electrical measurement techniques such as Deep Level Transient Spectroscopy or Admittance Spectroscopy to detect and characterize these recombination centers, as proposed in the 1970's [1,2]. These methods use the Shockley-Read-Hall (SRH) formalism for the representation of defects [3] in the simplest case. However, there is a need for methods able to probe the layers and stack before manufacturing the full device and making final contacts. Photoluminescence (PL) is a good candidate for such a goal, and one common way to probe recombination dynamics in thin-film solar cells or layer stacks is Time Resolved Photoluminescence (TRPL). With its sub-nanosecond resolution, it is clearly suited to direct bandgap thin-film semiconductors, where the apparent lifetimes range from a few ns to a few µs. Initially developed for the

* e-mail: baptiste.berenguier@cnrs.fr

characterization of III-V materials [4,5], it was then successfully applied to other materials, for example copper-indium-galium-di-Selenide (CIGS) [6–8] and more recently metal halide perovskites [9–11].

However, in a lot of cases, TRPL decays have complicated non-mono-exponential shapes. The interpretation is not straightforward [12], one needs to proceed to the study of several sets of decays for example as a function of temperature, illumination power, or bias voltage, or to correlate for example as a function of the results with other techniques such as PL quantum yields and current-voltage characteristics, and to use a mathematical modelling for the interpretation of the observed tendencies of the data sets. While transient techniques are dominating the contactless measurement of thin film recombination dynamics using Time Correlated Single Photon Counter (TCSPC) electronics, various frequency domain methods have also been used based on photoluminescence [13–21] or change of conductivity probed by microwave (known as microwave phase-shift [22–24]). One limitation of these methods is the frequency range that can be probed. Acquiring low-intensity modulated signals at high speed with an analog system is difficult since the electronic gain-band product limits the amplification of the signal. Reklaitis et al. [17] overcame this difficulty by using a photomultiplier and a fast laser diode and measured signals from 100 Hz to 100 MHz [17,25]. A second difficulty using modulated techniques on defective materials is that the signal can present a response that is not easy to interpret. For instance, such a signal when represented as a Bode diagram with phase and amplitude of the first harmonics versus modulation frequency can exhibit a non-monotonic behavior with "bumps", also called V-Shape patterns or V-Shapes, in contrast to MPL Bode plots recorded on silicon materials which exhibit Monotonic (decreasing) Shapes. Such behavior has been attributed to the response of defects [17,18], or to parasitic in-phase noise coming from a lack of laser filtering [17,25]. In addition to the mentioned techniques, non-linear heterodyne detection schemes have also been developed in the literature. Samples are illuminated with two lasers with slightly different modulation frequencies to create a beating effect in the response. This beating can be measured with slow devices such as ultra-sensitive lock-in amplifiers and cameras. Several harmonics are recorded, and it can be shown that some of them exhibit specific signatures in the presence of SRH levels [20,21]. While we recognize the full potential of the heterodyne scheme, it increases the complexity of interpretation. Furthermore, homodyne systems, i.e. with a single laser and a single modulation frequency have not been sufficiently studied, particularly regarding the appearance of V-Shape patterns in the Bode phase plot.

We recently developed a homodyne setup based on TCSPC electronics which is able to record modulated photoluminescence signals from 10 Hz up to 100 MHz [26]. We observed V-Shapes in the Bode phase plots in different semiconductors, and proposed the presence of SRH centers as an explanation [26]. Finally, Moron et al. proposed an analytical solution for explaining this behavior in the case of a CIGS-like p-type material including an acceptor SRH defect [27]. In line with this preceding work, the goals of the present article are (i) to verify the analytical calculation by parametric numerical studies, (ii) to take into account the effect of the defect density on the V-Shape appearance, (iii) to extend the study to undoped materials.

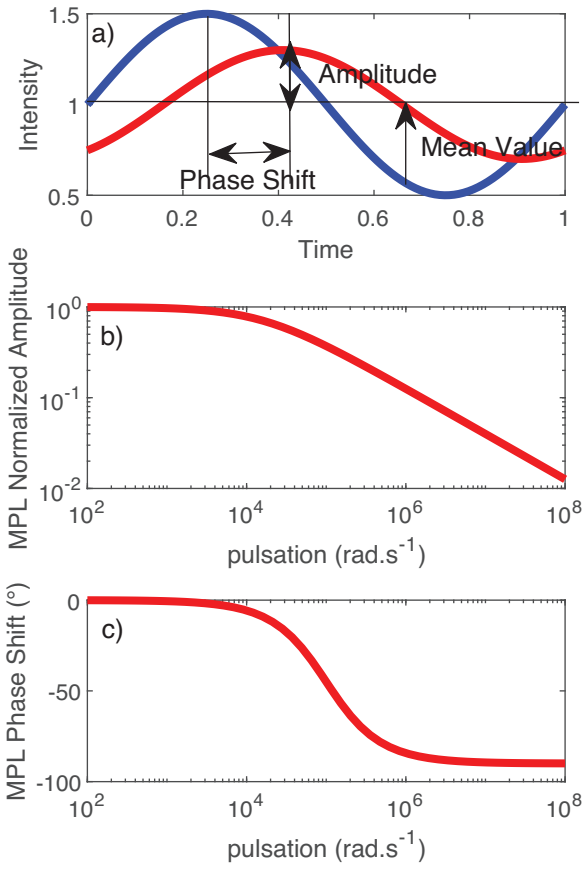

Fig. 1. Schematic of the different steps of an MPL experiment: (a) Laser (blue line) and PL (red line) sinusoidal signals at a given pulsation presenting a phase shift. (b) Example of a monotonic amplitude Bode plot; (c) corresponding phase Bode plot.

2 Analytical model

The MPL experimental principle and resulting data extraction are sketched on Figure 1. One illuminates the sample with an intensity modulated light and measures the resulting modulated PL signal. As we used a sinusoidally modulated illumination signal, the PL is periodic (Fig. 1a) and can then be expressed as a Fourier series. It is then possible to extract the mean value of the PL, as well as the amplitude and the phase shift (referred to the light excitation) of the PL first harmonic. Sweeping the modulation frequency, Bode plots of amplitude and phase of the fisrt harmonic can be recorded (Figs. 1b and 1c, respectively). In most previous studies (except [17,18]) the technique used low frequencies (below 1 MHz) and observed monotonic amplitude and phase behavior, as illustrated in Figure 1. However, it is possible to have non-monotonic behavior in different situations, as we will show.

We will now describe the fundamental equations governing the PL behavior in a thin semiconductor layer under a modulated illumination flux and including a single SRH center. In an opposite way to several studies, we will keep the dynamic form of SRH equations, which is necessary to model detrapping effects in a non-steady-state. In order to keep the problem simple enough to find analytical solutions, we neglect the possible effect of inhomogeneous illumination followed by diffusion and surface recombination and assume homogeneous carrier concentrations. This approximation holds if the layer is thin enough so that the carriers can homogeneize and redistribute rapidly at the scale of the period of modulation. In this case we have the following set of equations:

Carrier dynamics:

$$\frac{dn}{dt} = G - B_{rad}(np - n_{eq}p_{eq}) - C_n(N_t - n_t)n + e_n n_t \quad (1)$$

$$\frac{dp}{dt} = G - B_{rad}(np - n_{eq}p_{eq}) - C_p n_t p + e_p(N_t - n_t) \quad (2)$$

$$\frac{dn_t}{dt} = C_n(N_t - n_t)n - e_n n_t - C_p n_t p + e_p(N_t - n_t). \quad (3)$$

Electroneutrality:

$$p = C_{\text{static}} + n + n_t. \quad (4)$$

Optical generation rate:

$$G = G_0 + G_1 \sin(\omega t). \quad (5)$$

In these equations, n is the electron density, p the hole density, n_t the density of trapped electrons, $n_{(eq)}$ and $p_{(eq)}$ the values at equilibrium, N_t the density of defects at the energy E_t, C_n (C_p) the electron (hole) capture coefficient, i.e. the capture cross section σ_n (σ_p) multiplied by the thermal velocity v_n (v_p), e_n (e_p) the emission frequency of an electron (hole) to the conduction (valence) band. B_{rad} is the radiative recombination coefficient. C_{static} is a net static charge that depends on the doping, as calculated in appendix. G_0 and G_1 are the mean value and amplitude of the AC generation rate, and ω is the angular pulsation of the modulation.

The photoluminescence intensity, PL, is proportional to the radiative recombination rate:

$$PL = KB_{rad}np \quad (6)$$

where K is a proportionality factor accounting for the characteristics of the optical coupling from the PL emission to the detector. We also define the following rates.

Electron capture by the SRH defect:

$$Capture_n = C_n p_t n = C_n(N_t - n_t)n. \quad (7)$$

Electron emission by the SRH defect:

$$Emission_n = e_n n_t. \quad (8)$$

Hole capture by the SRH defect:

$$Capture_p = C_p n_t p. \quad (9)$$

Hole emission by the SRH defect:

$$Emission_p = e_p p_t = e_p(N_t - n_t). \quad (10)$$

Net radiative recombination rate:

$$R_{rad} = B_{rad}(np - n_{eq}p_{eq}) \quad (11)$$

and the expression of the SRH emission pulsations for electrons and holes toward the conduction band and valence band, respectively:

$$e_n = C_n N_c e^{(E_t - E_c)/k_b T} \quad (12)$$

$$e_p = C_p N_v e^{-(E_t - E_v)/k_b T}. \quad (13)$$

N_c (N_v) being the effective density of states in the conduction (valence) band. Taking into account equations (1)–(4) leads to an over-determined system of four equations for three unknowns (n, p, n_t). It is then possible to choose three of them, and the resolution we develop further will use equations (1) and (3) and (4).

In the present article, as in [28], we want to keep the solution fully analytical so we neglect harmonics other than the zero (mean value of the signal) and the first harmonic. Neglecting the high-order harmonics leads to the equation:

$$\begin{aligned} G &= G_0 + \frac{G_1}{2i}(e^{i\omega t} - e^{-i\omega t}) \\ &= G_0 + g_1 e^{i\omega t} + g_{-1} e^{-i\omega t}. \end{aligned} \quad (14)$$

We note that as G is a real signal, G_0 is real and the g_{-1} and g_1 terms are conjugated complex quantities. The same remarks hold for all the physical quantities here such as n, p, n_t. The equation system for the zero harmonic is presented in S1. Thus equations for the first harmonic will be:

$$\begin{bmatrix} A_{11} & A_{12} \\ A_{21} & A_{22} \end{bmatrix} \begin{bmatrix} n1 \\ n_{t1} \end{bmatrix} = \begin{bmatrix} g_1 \\ 0 \end{bmatrix} \quad (15)$$

with

$$\begin{aligned} A_{11} &= \Big(i\omega + B_{rad}(n_0 + p_0) + C_n(N_t - n_{t0})\Big) \\ A_{12} &= (B_{rad}n_0 - e_n - C_n n_0) \\ A_{21} &= \Big(C_p n_{t0} - C_n(N_t - n_{t0})\Big)\Big) \\ A_{22} &= \Big(i\omega + e_n + e_p + C_p(p_0 + n_{t0}) + C_n n_0\Big). \end{aligned} \quad (16)$$

We also remember that:

$$p_1 = n_1 + n_{t1} \tag{17}$$

and the equation governing the PL intensity for the DC and first harmonic parts are

$$I_{PL0} = KB_{rad}(n_0 p_0 + n_{-1} p_1 + n_1 p_{-1}) \tag{18}$$

and

$$\begin{aligned} I_{PL1} &= KB_{rad}(n_0 p_1 + n_1 p_0) \\ &= B_{rad}[(n_0 + p_0)n_1 + n_0 n_{t1}]. \end{aligned} \tag{19}$$

It is important here to make two remarks. First this complex matricial formalism is the counterpart of a time-domain matricial formalism as it has been established by Maiberg et al. [29]. Secondly this matricial formalism, either in time- or in frequency-domain could be extended to several trap levels provided we keep the small-signal approximation. In frequency-domain and for one single trap energy in the bandgap, the fist harmonic PL can be expressed as a function of the steady state quantities n_0, p_0, n_{t0},ω.

$$I_{PL1} = Kg_1 B_{rad}(n_0 + p_0)\frac{(i\omega + \omega_2)}{(i\omega)^2 + S(i\omega) + \omega_0^2} \tag{20}$$

with

$$\begin{aligned} \omega_2 = e_n + e_p + C_p p_0\left(1 + \frac{n_{t0}}{n_0 + p_0}\right) \\ + C_n n_0\left(1 + \frac{N_t - n_{t0}}{n_0 + p_0}\right) \end{aligned} \tag{21}$$

$$\begin{aligned} S = B_{rad}(n_0 + p_0) + e_n + e_p + C_p(p_0 + n_{t0}) \\ + C_n(n_0 + N_t - n_{t0}) \end{aligned} \tag{22}$$

and

$$\begin{aligned} \omega_0^2 = \Big(B_{rad}(n_0 + p_0)\omega_2 + (C_p n_{t0})(e_n + C_n n_0) \\ + \Big(C_n(N_t - n_{t0})\Big)\Big(C_p(p_0 + n_{t0}) + e_p\Big). \end{aligned} \tag{23}$$

Under the previous assumptions, and as noticed before by Moron et al. [27,28]. the phase and amplitude of the PL first harmonic with respect to the generation rate can be expressed as:

$$\phi_1 = -arctan(\omega/\omega_1) + arctan(\omega/\omega_2) - arctan(\omega/\omega_3) \tag{24}$$

$$\begin{aligned} \rho_1 = Kg_1 B_{rad}(n_0 \\ + p_0)\frac{\omega_2}{\omega_1\omega_3}\sqrt{\frac{\left(1 + \left(\frac{\omega}{\omega_2}\right)^2\right)}{\left(1 + \left(\frac{\omega}{\omega_1}\right)^2\right)\left(1 + \left(\frac{\omega}{\omega_3}\right)^2\right)}} \end{aligned} \tag{25}$$

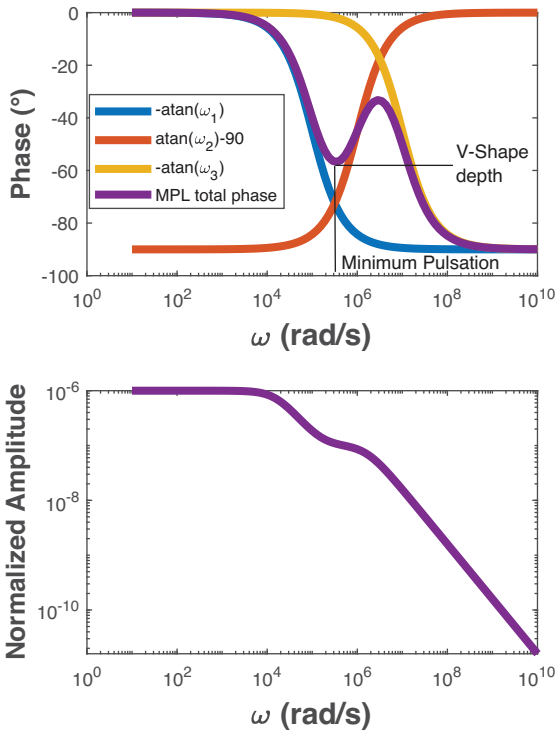

Fig. 2. (a) Scheme of the principle of V-Shape formation due to three contributions in the phase Bode plot; (b) the corresponding amplitude Bode plot.

with

$$\omega_1 = \frac{S - \sqrt{S^2 - 4\omega_0^2}}{2} \tag{26}$$

$$\omega_3 = \frac{S + \sqrt{S^2 - 4\omega_0^2}}{2}. \tag{27}$$

The three pulsations ω_1, ω_2, ω_3 are called corner pulsations of the Bode plot. Since there is a coupling between the zero order and the first harmonic in equation (18), the three pulsations are supposed to depend on ω except in the case of sufficiently small modulation or sufficiently low injection as in reference [28]. In other cases, the system has to be solved numerically rather than analytically to find the solution.

The sum of the three artangent functions in equation (24), one of them having an opposite sign compared to the two others, produces a typical phase pattern in the frequency dependence, as presented in Figure 2 that we called V-Shape, as well as an amplitude Bode plot exhibiting three domain with different slopes. This is the main signature of a SRH defect on the MPL signal and it cannot be produced by radiative or Auger recombinations. This indicates that the carrier dynamics cannot be described anymore by a single pulsation (or lifetime) since several frequency-dependent recombination rates involving three carriers population (free holes, free electrons and

trapped electrons) are in competition. Furthermore, Moron et al. [27] distinguished two cases of V-Shapes. In the low injection case, "low injection" being defined below, V-Shapes are exclusively due to the competition of radiative recombination and minority carrier re-emission as in [29]. However, in an intermediate, so-called middle injection regime, V-Shapes can appear also by the competition between radiative and SRH recombination. Experimentally, the low injection V-Shape should be stable when reducing the laser flux while the middle injection one should disappear.

We remark that the quantity ω_2 is similar to the inverse of the time constant defined in the analysis of admittance spectroscopy, defined by Losee as $\tau^{-1}=C_n\, n_0+C_p\, p_0+e_n+e_p$ [2] which governs the frequency dependence of the capacitance and has to be distinguished from SRH lifetimes. Thus, we are developing a kind of contactless admittance spectroscopy. Experiments measuring MPL pulsations versus temperature are beyond the scope of the article, but may be carried out soon.

2.1 Modulated photoluminescence signal in the case of a single defect in a p-doped layer: analytical simplifications at low injection

In this subsection we first consider a defect in a p doped material with majority carrier concentration at equilibrium p_{eq}, and submitted to a low illumination. In [28], Moron et al. proposed a definition of the low illumination case, which is equivalent to the condition $n_0 << p_{eq}$ together with at least one of the condition $n_{t0} << min(N_t, p_{eq})$ or $n_{t1} << n_{t0}$.

The authors showed that under such conditions, and even with strong modulation ratios, the coupling between the harmonics zero and one disappears, $n_{-1}\, p_1$ and $n_1\, p_{-1}$ are negligible with respects to $n_0 n_0$. The same holds for the other first harmonic products present in equations (24), (26) and (27) with respect to their respective zero order products.

I_{PL1} can be simplified, depending on the position of the energy level of the SRH center in the bandgap. They defined two energy levels:

$$E'_F = E_F + k_b T ln(1 + N_t/p_{eq}) \tag{28}$$

$$E^*_F = E_i + (E_i - E_F) - k_b T ln(C_n/C_p). \tag{29}$$

$E_{F\prime}$ corresponds to the energy where the occupation of the defect at equilibrium is equal to the minimum of (N_t, p_{eq}), p_{eq} being the equilibrium majority carrier concentration. E^*_F is the energy where the emission rate of trapped electrons becomes stronger than that of the capture of holes from the valence band. Please note that E^*_F is dependent on the capture cross sections and can lies outside the bandgap for some specific cases. They defined four scenarios for this low injection condition:

– Scenario 1: $E_t > E^*_F$ and $C_n\, N_t < B_{rad} p_{eq}$, negligible electron trap. Approximations imply that $\omega_2 = e_n$ and is equal to ω_1 or ω_3 so that the MPL phase reduces to a single arctangent function involving the radiative lifetime:

$$\phi = arctan\Big(\omega/(B_{rad} p_{eq})\Big). \tag{30}$$

– Scenario 2: $E_t > E^*_F$ and $C_n\, N_t > B_{rad}\, p_{eq}$, non negligible electron trap. Approximations imply that $\omega_2 = e_n$. The formula for the two other corner pulsations of I_{PL1} are presented in S2.

– Scenario 3: $E_{F\prime} < E_t < E^*_F$, recombination center. Approximations imply that ω_2 is equal to ω_1 or ω_3, the MPL phase reduces to a single arctangent function:

$$\phi = arctan\Big(\omega/\Big(C_n(N_t - n_{t0}) + B_{rad} p_{eq}\Big)\Big). \tag{31}$$

– Scenario 4: $E_t < E^*_F$ and $E_t < E_{F\prime}$, hole trap. Approximations imply that ω_2 is equal to ω_1 or ω_3, the MPL phase reduces to a single arctangent function:

$$\phi = arctan\Big(\omega/\Big(c_n(N_t - n_{t0}) + B_{rad} p_{eq}\Big)\Big). \tag{32}$$

Scenario 4 may seems similar to scenario 3. However, it relies on the assumption $n_{t1} << n_{t0}$ when the three previous scenarios rely on $n_{t0} << min(N_t, p_{eq})$. We call the corner pulsations resulting from the resolution of equations (24), (26) and (27) "analytical results" and those using simplified equations (30)–(32) and (S10–S11) "low injection" results.

2.2 One supplementary limit between V-Shape and Monotonic-Shape at low level density

The low injection model for doped materials gives an energy limit E^*_F for the defect level that separates the Bode phase plot between V-Shapes and Monotonic Shapes curves , and which is independent of the defect density, except if the SRH recombination become negligible in compare to radiative recombination. We would like to present another limit, which is useful for any doping level and is defect density dependent.

If the defect density is sufficiently small and as the injection level increases, we will get:

$$\begin{aligned} &B_{rad}(n_0 + p_0) + (e_n + e_p + C_n n_0 + C_p p_0) \\ &\quad \gg [C_n(N_t - n_{t0}), C_p n_{t0}]. \end{aligned} \tag{33}$$

Then two limiting cases can occur depending of the defect parameters. In the first limiting case where $B_{rad}\ (n_0 + p_0) << (e_n + e_p + C_n\ n_0 + C_p\ p_0)$:

$$S \approx \omega_2 \approx (e_n + e_p + C_n n_0 + C_p p_0) \tag{34}$$

$$\omega_0^2 < S\Big(B_{rad}(n_0 + p_0) + C_n(N_t - n_{t0}) + C_p n_{t0}\Big) << S^2 \tag{35}$$

under these assumptions,

$$\omega_1 \approx \frac{\omega_0^2}{S} \tag{36}$$

Table 1. Parameters used for the model.

Material	CIGS	Perovskite
Generation rate G_0 (cm^{-3} s^{-1})	1.8×10^{18}	
Modulation ratio G_1/G_0	0.05 or 1	0.05 or 1
Bandgap E_g (eV)	1.2	1.5
Equilibrium holes density P_{eq} (cm^{-3})	3.10^{16}	n_i
Conduction band density of states N_c (cm^{-3})	2×10^{18}	2.2×10^{18}
Valence band density of states N_r (cm^{-3})	2×10^{18}	1.9×10^{19}
Radiative recombination coefficient B_{rad} (cm^3/s)	8×10^{-11}	10^{-10}
k_BT (eV)	0.0258	
N_t (cm^{-3})	from 1×10^{12} to 1×10^{17} by decade	
C_n ($cm^3 s^{-1}$)	from $1{\times}10^{-15}$ to $1{\times}10^{-7}$ by decade	
C_p (cm^3 s^{-1})	from $1{\times}10^{-15}$ to $1{\times}10^{-7}$ by decade	
$E_t - E_v$ (cm^3 s^{-1})	varied from 0.05 eV to $E_g - 0.05$ eV in eleven equal steps	

$$\omega_3 \approx S \approx \omega_2 \tag{37}$$

$$\omega_{eff} = B_{rad}(n_0 + p_0) + C_n(N_t - n_{t0})\frac{C_p p_0 + e_p}{S} + C_p(n_{t0})\frac{e_n + C_n n_0}{S}. \tag{38}$$

If there is no electron re-emission and very low minority carrier injection, as in the previous section:

$$\omega_1 = B_{rad}(n_0 + p_0) + C_n(N_t - n_{t0}). \tag{39}$$

In the second limiting case: $B_{rad}\ (n_0{+}p_0) \gg (e_n{+}e_p{+}C_n n_0{+}C_p\ p_0)$

$$S \approx \omega_2 \approx B_{rad}(n_0 + p_0) + (e_n + e_p + C_n n_0 + C_p p_0) \tag{40}$$

$$\omega_0^2 \approx (e_n + e_p + C_n n_0 + C_p p_0)\Big(B(n_0 + p_0)\Big). \tag{41}$$

We deduce that $\omega_3 = \omega_2$ or $\omega_1 = \omega_2$ and the remaining pulsation is equal to $B_{rad}\ (n_0{+}p_0)$. This explains the non-appearance of V-Shapes in MPL experiments involving materials such as silicon, whose purity is a lot higher than most of thin film materials, with defect densities several orders of magnitude lower.

3 Parametric study over the four defect parameters for a single defect at low laser fluxes

At this point of this article, we aim to further investigate the appearance of V-Shapes and Monotonic-Shapes in a given material. Which kind of qualitative and quantitative information can we extract from an MPL curve? Furthermore, as we said previously, our setup is using large modulation ratios close to unity. Our model is neglecting the possibles harmonic. Does the modulation ratio influence the results?

To reach this goal, we perform a parametric numerical study over the four defect parameters, firstly in a p-type CIGS-like material using the previous ground equations (1)–(13), secondly for an intrinsic perovskite-like material. The parameters are summarized in Table 1. Two calculation paths are compared.

Firstly, we aim to produce a data-set without analytical simplifications, supposed to represent as close as possible the experiments in thin uniform films. Equations (1), (2), (3), are solved numerically and with respect to time with Matlab ODE15s function: (i) the initial equilibrium state is calculated to ensure electroneutrality as calculated in Appendix; (ii) then the time-dependent response to a modulated generation rate is calculated over enough periods to ensure the stability of the solution; (iii) once the computed result is temporally stable, we select a period and the continuous part as well as the phase and amplitude of the first harmonic of the PL are computed via a Fourier transform. Indeed, the solutions of this parametric study are totally "numerical results". An example of the obtained curves is presented in S3.

Secondly, using analytical model, we calculate the mean value of the carrier density at steady-state using equations (7) and (8) and then the first harmonic characteristic pulsations ω_1, ω_2, ω_3 using equation (20).

Thirdly, we calculate the last set of pulsations $\omega_1, \omega_2, \omega_3$ using low-injection results.

In the next subsection we will investigate the correlation between numerical (Eqs. (1)–(4), analytical (Eqs. (23) and (26), (27)) and simplifed low-injection results (Eqs. (30)–(32) and (S10–S11)).

3.1 Small-signal conditions

3.1.1 P-type material

The first numerical results use a modulation ratio of 5 percent of the mean light power. The mean generation rate is fixed to $1.8{\times}10^{18}$ $cm^{-3}.s^{-1}$. This corresponds to a photon flux of 10^{14} photons/cm^2/s in a 500 nm thick layer with an absorption coefficient of $5{\times}10^4$ cm^{-1}. This keeps the

injection range in the small signal approximation and ensures the condition $n_0 < 8\times10^{11}$ cm$^{-3} << p_{eq}$ since the radiative lifetime is close to 400 ns and the mean carrier density is smaller than the product of generation rate by radiative lifetime. We simulated 5832 cases corresponding to 12 trap energies, 6 defect densities and 9 capture coefficients for both types of carriers. The trap energies are covering the whole bandgap and are regularly spaced. The capture coefficients are spaced logarithmically by decades. C_n (respectively C_p) starts from 1×10^{-15} cm^3/s. Assuming a thermal velocity of 10^7 cm/s equal for both types of carriers this correspond to a capture cross-section of 10^{-22} cm^2 which is an extremely small value. It rises to 10^{-7} cm^3/s, corresponding to a capture cross-section of 10^{-14} cm^2 which is a large value owing to the literature. In the same way, the trap density (N_t) values are chosen using a logarithmic span from insignificant densities to densities strongly affecting the material. A good way to illustrate the span in parameters is to consider SRH lifetimes that we can formulate as $\tau_{n,p}=1/(C_{n,p}\, N_t)$. The SRH lifetimes are thus covering a vey large interval ranging from 10^3 s to 10^{-10} s.

Once the experiments are simulated, we perform an automatic data treatment in the following way . First, we try to perform a numerical adjustment procedure (fitting) of each phase curve with a single arctangent function *atan* (ω/ω_{eff}). We impose the maximal phase error on one point to be 3 degrees and also check the absence of sign change in the derivative. If the fit is successful (error for each point inferior to 3 degrees) and no sign change is present in the derivative, the curve is classified as Monotonic-Shape case. If the test is not successful we try to fit the same curve with the sum three arctangent functions with three corner pulsations, as a V-Shape with the same error required (formula (24)). If successful the curve is classified as a V-Shape case. If not successful, the curve is classified as "Unknown". We observed by plotting the curves that the "Unknown" curves are mainly distorted curves due to algorithm convergence failures.

For the 5832 cases, we found 817 V-Shape cases, 4894 Monotonic-Shapes and 121 "Unkown" distributed according to the four scenarios. The repartition of V-Shapes and Monotonic-Shapes over the four scenarios is displayed in a pie chart in Figures 3a and 3b respectively. For V-Shape case, 73 belong to scenario 1, 99 to scenario 2, 605 to scenario 3 and 40 to scenario 4 whereas for the Monotonic Shape case, 392 belong to scenario 1, 77 to scenario 2, 3982 to scenario 3 and 443 to scenario 4. Supposing that the low injection regime is fulfilled, the results for V-Shape cases are not in agreement with the simplified model since the V-Shape are supposed to only be generated in the scenario 2 conditions. In order to investigate these phenomena, we will answer several questions.

The first question: we have to answer regarding the data from numerical simulations is to understand when the V-Shapes appear. From the dependence of V-Shape cases on the various trap parameters shown in Figure S4 can note the following:

– Histogram (a), the number of V-Shapes is increasing with the defect density. There is no V-Shapes for $N_t < 10^{13}$ cm^{-3} s^{-1}. When $N_t <= 10^{17}$ cm^3 s^{-1}, 35 % of the curves present a V-Shape.

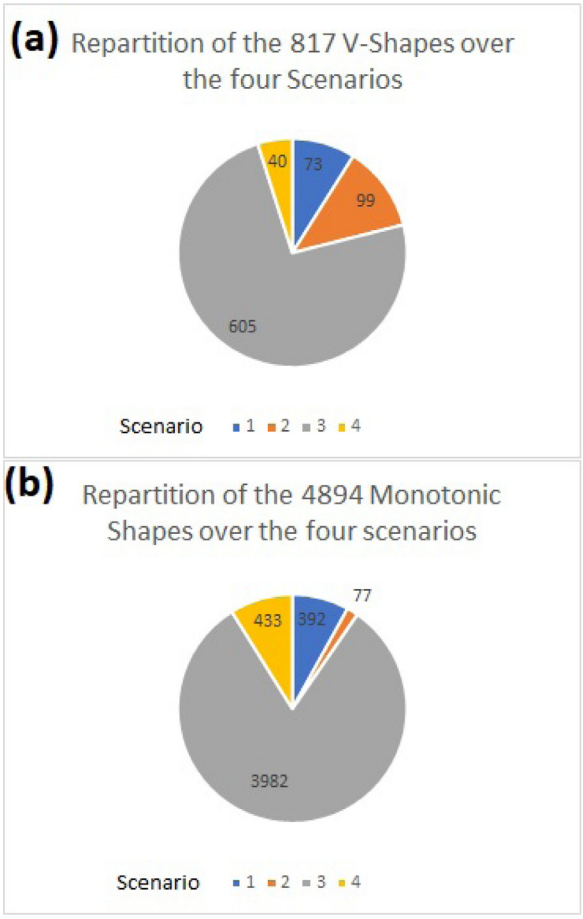

Fig. 3. (a) Repartition of V-Shape cases (a) and Monotonic-Shapes (b) over the four scenarios.

– Histogram (b), V-Shapes appear at each energy.
– Histogram (c), V-Shapes correspond to electron capture coefficients C_n greater than 10^{-12} cm^3 s^{-1}, the number of V shapes increases with C_n.
– Histogram (d), the probability of appearance V-Shapes increases when the holes capture cross-section decreases.
– Histogram (e), the ratio between C_n and C_p has to be greater than 0.01 and the increase of this ratio increases the probability of appearance of the V-Shapes. The mean and standard deviation of decimal logarithm of these two parameters are 3.59 and 2.21 respectively. A remark is that the natural spreading of all the data-set for the logarithm of this ratio is centered on 0 with standard deviation 3.65 due to the chosen spans of C_n and C_p. Thus, a high ratio facilitates the apperance of V-Shapes.

From the dependence of Monotonic-Shape cases on the various trap parameters shown in Figure S5, one can note the following:

– Histogram (a), the occurence of Monotonic Shapes is decrease when the defect density increases.
– Histogram (b), each energy can possibly give a monotonic behaviour.

– Histograms (c) and (d), the occurrence is strong whatever the electron or hole capture coefficient value.
– Histogram (e), the logarithm of the ratio between C_n and C_p is centered on –0.75 with standard deviation 3.36. Monotonic Shapes do not need a high ratio to appear.

As an answer to this first question we note that a high defect density and a high C_n/Cp ratio are the most important factors for the V-Shape appearance.

The second question: is the correspondence between the analytical results and the numerical ones. In the case where a Monotonic-Shape is detected in numerical results we notice that two pulsations of the analytical model are equal (ω_1=ω_2 or $\omega_3 = \omega_2$), and we choose to set the remaining pulsation ω_{eff} to the value (between ω_1 or ω_3) that does not equal ω_2. Then we compare the remaining pulsation ω_{eff} to the fitted one on Figure S6. We can notice a remarkable correspondence between the two sets of values for Monotonic Shapes. In the case of V-Shapes we can observe a relative discrepancy between predicted and fitted values as seen in Figure S7. Of course, most of the values are close to the y=x axis and the model is therefore relevant. But for ω_1 or ω_2 we can observe that several points are far away from the line. If we arbitrarily choose a threshold of 2 for the ratio between calculated and fitted omegas ($|log_{10}\left(\frac{\omega_{i_{\text{fit}}}}{\omega_{i_{\text{calculated}}}}\right)| < 0.3$), 319 values of fitted ω_1, 336 of ω_2, and 25 of ω_3 are not corresponding to analytical ones. When we studied this discrepancy, we noticed than the V-Shapes were either extremely small (the depth of the local dip producing the V-Shape is less than 1 degree, the curve exhibits a kind of kink rather than a marked V-Shape), or that the characteristic frequencies were outside the domain of frequencies we used, leading in both cases to an error in the fit. We will provide more details below.

As a third point of investigation, we focus on the results of the low injection model. The correlation between low injection model and numerical simulation is nearly perfect as seen in figures S8 and S9 for the 99 predicted V-Shapes in scenario 2, and for the 4817 Monotonic Shapes belonging to scenarios 1,3 and 4. All curves predicted by the low injection model have the right characteristic corner pulsations. However, there are only 99 V-Shapes corresponding to this case defined by $E_t > E_F^*$ and $C_n N_t >> B_{rad}\, p_{eq}$ (For the second inequality we chose to select all the curves where $C_n N_t > B_{rad} p_{eq}$). 718 supplementary V-Shapes are not predicted by low injection model but whose analytical pulsations and fitted pulsations are in accordance with scenarios 1 (68), 3 (605) and 4 (40). The common point between these non predicted V-Shapes is that ω_1 is really close to ω_2. In 96% of cases the ratio between the two pulsations is inferior to two. Then we checked the hypotheses of the article [28] which are summarized in Table 2. These hypotheses are:
– Order 0 not varying with ω.
– Second harmonic negligible.
– Low injection approximation as defined before.
– Phase of the PL equal to the phase of electron density.

We noticed that the low injection condition, as well as other hypotheses, are dependent on the numerical criterion we chose for probing the validity of the hypothesis. For example, we consider the relationship $n_{t0} \ll min(N_t, p_{eq})$ or $n_{t1} \ll n_{t0}$. Supposing it numerically means $n_{t0} < 10^{-3} \times \min(N_t, p_{eq})$ or $n_{t1} < 10^{-3} \times n_{t0}$ (0.1% threshold), we observe that 65% of V-Shapes are "middle injection" V-Shapes as predicted in [27]. Supposing a criterion of 10^{-5} will bring the proportion of "middle injection V-Shape" at 92%. Reducing the injection sufficiently should make the V-Shape disappear in the case of a deep trap. The main reason for the appearance of non-predicted V-Shapes is that the low injection condition is violated. Then, we cannot determine the trap energetic position in the bandgap only by the appearance or disappearance of V-Shapes.

Table 2. Verification of assumptions.

Hypothesis	
Mean value varying more than 1% with ω	35%
Second harmonic greater than 2% of the mean value	5%
Low injection approximation violated (0.1% threshold)	65%
Phase of PL different than Phase of electron density	0%

We show that we may distinguish between the two kinds of V-Shapes by the depth of the minimum of the phase. We define this minimum frequency by the zero of the derivative of the two first arctangents:

$$\frac{1}{\omega_2\left(1+\left(\frac{\omega_{min}}{\omega_2}\right)^2\right)} - \frac{1}{\omega_1\left(1+\left(\frac{\omega_{min}}{\omega_1}\right)^2\right)} = 0. \quad (42)$$

We then calculated the phase at ω_{min} using the analytical data set. The result is plotted on Figure 4. In order to make the interpretation easier, we used the Matlab function ksdensity, which involves one or several normal kernel smoothing functions to calculate an estimation of the two parameters probability density function representing the results. Then we plotted iso-lines of the resulting kernel density function for each scenario. On each graph, there are four concentric zones centered around the kernel density function maxima, the darkest corresponding to 20% of probability for the pulsation to be found in this area, the second concentric zone 40% of probability, then 60%, 80%. The purpose of this data treatment is to surround by dark (respectively light) zones the high (respectively low) concentration of points. We can remark that below ω_{min}=10^8 rad.s^{-1} the V-shapes of scenario 2 (a) on one hand and the V-shapes of scenarios 1 (b), 3 (c) and 4 (d) on the other hand present separated domains. The former have a minimum below 25 degrees when the latter have most of their points above this limit. Of course, this limit may be dependent on the injection level and the calculation should be conducted again at a given experimental working point.

The conclusion of this third point is the following: the limit where the carrier injection enters the "low injection" domain as defined at the beginning of 2.1 is not sharp, and therefore the validity range of the simplified low injection

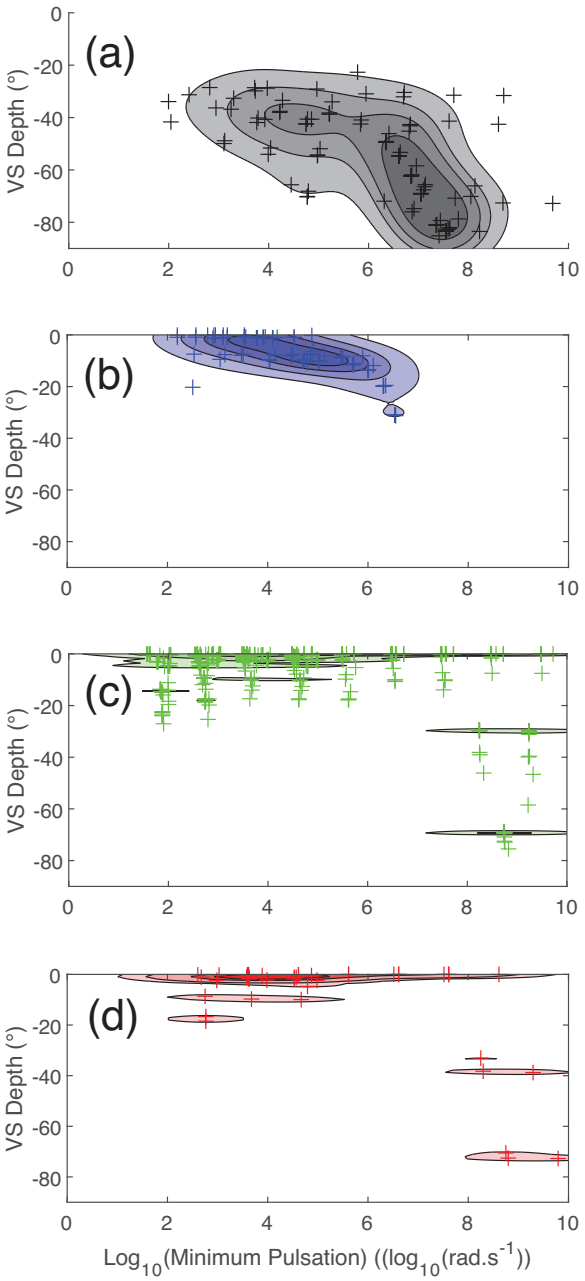

Fig. 4. P-doped small-signal case: frequency and depth of the phase minimum of the V-Shapes for (a) V-Shape belongings to scenario 2, (b) V-Shapes belonging to scenario 1, (c) V-Shapes belonging to scenario 3, (d) V-Shapes belonging to scenario 4. A kernel density treatment has been used to visualize the areas with strong crosses densities (see details in the text). The crosses are the result of the analysis using formula (42) of numerical results for all the observed V-Shapes.

model is to be considered with care, since the numerical signification of the inequality << is unclear. Experimentally, low injection and middle injection V-Shapes can be distinguished by reducing the illumination. If a V-Shape at a certain illumination flux remain unchanged at lower illumination, it imply that the low injection is reached. However the experimental noise may prevent to reach this regime. Then, the VS originating from low injection regime and a significant trap density (such as it does not belong to scenario 1) can be distinguished from the other scenarios by the depth of the phase minimum, wich should be below -25 degrees of phase.

As a fourth point, we aim to verify the influence of trap density on the appearance of V-Shapes . We define two ratios:

$$Ratio_1 = \frac{C_p n_{t0}}{\left(e_n + e_p + C_n n_0 + C_p p_0 + B_{rad}(n_0 + p_0)\right)} \quad (43)$$

$$Ratio_2 = \frac{C_n(N_t - n_{t0})}{\left(e_n + e_p + C_n n_0 + C_p p_0 + B_{rad}(n_0 + p_0)\right)}. \quad (44)$$

These ratios define the limits of validity for the conditions of inequality (32) of Section 2.2. In Figure 5 we represent the correlation between $Ratio_1$ and $Ratio_2$ for each element of the data set subdivided into the four scenarios. As dark blue crosses, V-Shapes corresponding to scenario 2. As cyan crosses V-Shape corresponding to other scenarios. In red crosses Monotonic Shapes corresponding to scenario 2, as magenta crosses Monotonic Shapes corresponding to other scenarios. $Ratio_2$ is a main criterion for the apparition of V-Shape. If too small (<0.01), there is no V-Shape as predicted previously. $Ratio_1$ is always smaller than unity in our case. Indeed, the trap density is playing a crucial role in the appearance of V-Shapes as predicted in Section 2.2.

3.1.2 Intrinsic material

In this simulation, we chose a Perosvkite-like material with intrinsic doping properties. The parameters used for the model are in Table 1. We kept the modulation ratio to 5 percent ensuring small-signal condition. In this section, we use the same procedure as for CIGS p-type material. We carry out a fit of the curves, following the same data treatment as in the previous section. We observe for the phase curves 988 V-Shapes, 4400 Monotonic Shapes, 444 "Unknown" curves. For clarity all the graphs are given in the Supplementary Information. For the V-Shape appearance with respect to the SRH parameters, we observe the following facts in Figure S10:

- Histogram (a), the number of V-Shapes is increasing with the defect density. There is no V-Shapes for N_t<10^{13} cm^{-3} and 429 for N_t<=10^{17} cm^{-3}.
- Histogram (b), there are V-Shapes for any energy level, with a maximum of occurrence at the middle of the gap.
- Histograms (c) and (d), the number of V-Shapes increase with the capture coefficients and stays approximatively constant above 10^{-10} cm^3/s^{-1}.
- Histogram (e), the optimal ratio between C_n and C_p is one (the mean value of the decimal logarithm is zero and the standard deviation 2.8).

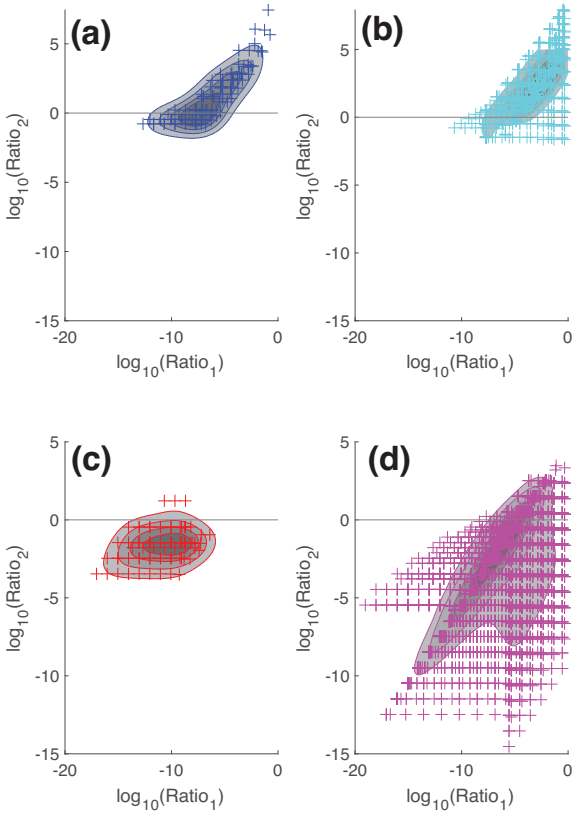

Fig. 5. p-type small-signal case: appearance of V-Shapes and Monotonic-Shapes curves with respects to $Ratio_1$ and $Ratio_2$ for the four scenarios. (a) Dark blue crosses: V-Shapes corresponding to scenario 2. (b) Cyan crosses: V-Shapes corresponding to other scenarios. (c) Red crosses: Monotonic-Shapes corresponding to scenario 2. (d) Magenta crosses: Monotonic-Shapes corresponding to other scenarios. A kernel density treatment has been used to visualize the areas with strong point densities (see details in the text).

– Histograms (f) and (g), the occurrence of V-Shapes increases with the product of defect density and electron or hole capture coefficient.

Clearly, the main reason for the appearance of V-Shapes is the ability of the defect to capture both type of carriers and proceed to recombination. Regarding the occurence of Monotonic-Shapes, Figure S11 confirms that it is reduced (V-Shapes is increased by the increase of defect density (a) and capture cross sections (b and c). The optimal ratio between capture cross sections is also one, as for the V-Shapes but the standard deviation of the logarithm of the ratio is greater (3.7) and the occurence of Monotonic-Shapes is larger than that of the V-Shapes (e).

Figure S12 and S13 show perfect correspondence between analytical model and simulations. The deviations, 67 for ω_1, 92 for ω_2 in the case of V-Shapes, 30 for ω_3, in the case of Vshapes , and 15 for Monotonic-Shapes are also due to fit failures.

Finally, Figures S14 and S15 give more information about the condition of appearance of each type of curve shape . For the appearance of V-Shapes, on Figure S14 we can observe that:

– Histograms (a) and (b), in most of V-Shape cases, the emission of one t type of carrier is negligible compared to the capture of the other type of carrier. The mean values for (a) and (b) are 7.25 and 6.85 (in log) and the standard deviation is 6. There are few points below zero and no one below -5. This implies that the defects are recombination centers rather than shallow traps experiencing trapping and emission phenomena.
– Histograms (c) and (d), The capture mechanisms are dominant with respect to the radiative recombination. (Mean 2.4 and standard deviation 2.6).
– Histograms (e) and (f),the net recombination rates are dominant with respect to the radiative recombination rate (Mean 2.15, standard deviation 2.8).
– The recombination rates for electrons and holes are the same, we are in stationary regime.

For the appearance of Monotonic Shapes cases, in Figure S15 we can observe that:

– Histograms (a) and (b), the fact that the re-emission is dominating the recombination does not play a significant role.
– Histograms (c) and (d), (e) and (f), the radiative recombination is dominating the trap-assisted one, with or without taking the re-emission into account. For (c) and (d) the means are –3 and standard deviations 2.7. The recombination rates for electrons and holes are the same.

Finally, we plot the ratios 1 and 2 as in the p-type case and observe on Figure 6 that the lines where $ratio_1$=1 and $ratio_2 = 1$ are as predicted separating the apparition of V-Shapes (blue cross) and Monotonic-Shapes (red circles) on Figure 6.

We conclude from these figures than the V-Shapes will appear in an intrinsic material as soon as the net recombination rates for the defect is larger than the radiative recombination rate and when the defect density is sufficient with respect to ratios 1 and 2.

3.2 Large-signal conditions

In this section we aim to understand how far the characteristic pulsations are modified by the large modulation (i.e. G_1=G_0). In the case of the p-type material, the two groups of pulsations match quasi perfectly as presented on Figure S16, proving that the large-signal does not affect the response of the material. For the intrinsic case, there are 998 V-Shapes for the small signal case and 1169 for the large-signal case. The V-Shapes which are detected under small-signal but not under large-signal (46 cases) are mainly Monotonic-Spahes with small deformation which were not detected by the first step of the algorithm. 227 V-Shapes were associated with large signal and not with small-signal. Among them 162 were distorted in case of small-signal and classified as “unknown” and 65 were Monotonic-Shapes but not detected by the first step of

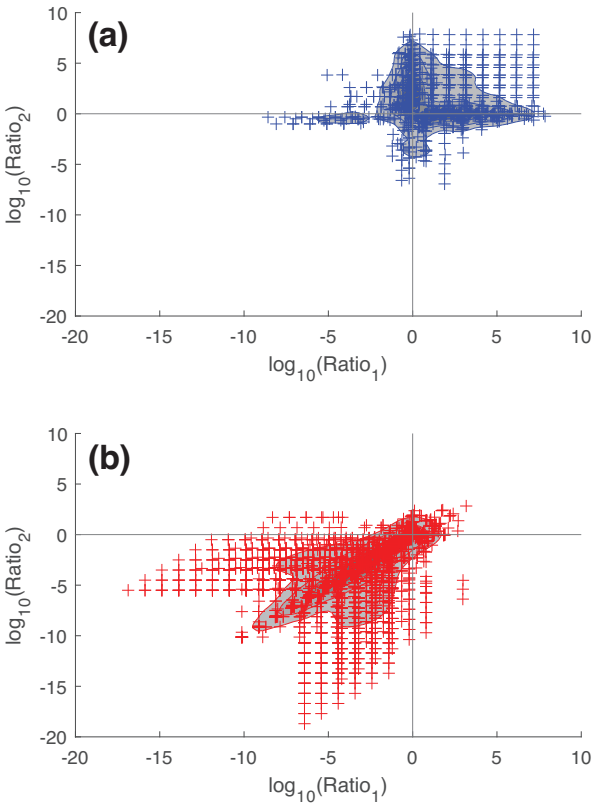

Fig. 6. Intrinsic small signal case: appearance of (a) V-Shapes (blue crosses) and (b) Monotonic-Shapes (red crosses) with respect to $Ratio_1$ and $Ratio_2$. The same kernel density treatment has been used to visualize the areas with strong point densities.

the algorithm. The common cases between small and large-signal exhibit the same pulsation. We thus emphazise that the large signal does not affect the pulsation detected for an experiment.

4 Conclusion

We previously developed an analytical model for MPL spectra in the case of a p-doped semiconductor. It predicts the appearance of V-Shapes in the Bode phase plot under certain conditions and Monotonic-Shape behavior otherwise. The equations were reformulated in a more explicit way and several new relationships were found allowing us to explain the disappearance of V-Shape cases at low defect densities. The analytical model was checked against fully numerical simulations for a single defect state and we tested 5832 cases corresponding to a wide spread of defect parameters values. This led to mapping the material parameter space, and determining where V-Shapes can occur or not. Cases where the analytical model is applicable could be determined. Discrepancies were found with some approximations of the analytical model in the case of low injection. The low injection limit is dependent on the chosen numerical criterion. If the injection is not sufficiently low, one can define a kind of "middle injection" regime where V-Shapes may still exist, however with a less pronounced depth compared to really low injection. We also studied the effect of the modulation ratio covering small-signal to large-signal conditions. Modulation ratio seems to have no impact on the MPL phase shape results of the tested 5832 cases. Finally, we developed numerical modelling for intrinsic materials, showing that V-Shapes can also be observed, and we related the trends for such observation with the material parameters.

Acknowledgments

We acknowledge Nicolas Moron for the discussions during his PhD. We aknowledge Daniel McDermott for gentle proofreading.

Funding

The study was supported by the IPVF CHARMING program in the frame of the french national "Investissements d'Avenir" program(ANR-IEED-002-01).

Conflicts of interest

There is to our knowledge no conflict of interest related to this article.

Data availability statement

The datasets used and/or analysed during the current study are available from the corresponding author on reasonable request.

Author contribution statement

Alban Asseko wrote the program in order to calculate the datasets, under the direction of Baptiste Berenguier and Jean-François Guillemoles. Baptiste Bérenguier performed both the analytical and numerical calculation, analysed the data, and drafted the article. Hiba Hadara made some verification of the calculation truthfulness. Sylvain Le Gall, Jean-Paul Kleider, Jean-François Guillemoles provided critical feedback and contributed to the redaction of the article.

Supplementary material

Supplementary Material provided by the author.

The Supplementary Material is available at https://www.epj-pv.org/10.1051/epjpv/2024045/olm.

References

1. D.V. Lang, Deep-level transient spectroscopy: A new method to characterize traps in semiconductors, J. Appl. Phys. **45**, 3023 (1974)
2. D.L. Losee, Admittance spectroscopy of impurity levels in Schottky barriers, J. Appl. Phys. **46**, 2204 (1975)

3. W. Shockley, W.T. Read, Statistics of the recombinations of holes and electrons, Phys. Rev. **87**, 835 (1952)
4. R.K. Ahrenkiel, Measurement of minority-carrier lifetime by time-resolved photoluminescence, Solid State Electron. **35**, 239 (1992)
5. Y. Rosenwaks, Y. Shapira, D. Huppert, Picosecond time-resolved luminescence studies of surface and bulk recombination processes in InP, Phys. Rev. B **45**, 9108 (1992)
6. D. Kuciauskas, J.V. Li, M.A. Contreras, J. Pankow, P. Dippo, M. Young, L.M. Mansfield, R. Noufi, D. Levi, Charge carrier dynamics and recombination in graded band gap CuIn_(1-x) Ga_x Se_2 polycrystalline thin-film photovoltaic solar cell absorbers, J. Appl. Phys. **114**, 154505 (2013)
7. M. Maiberg, T. Holscher, S. Zahedi-Azad, W. Franzel, R. Scheer, Investigation of long lifetimes in Cu(In,Ga)Se_2 by time-resolved photoluminescence, Appl. Phys. Lett. **107**, 122104 (2015)
8. G. El-Hajje, D. Ory, M. Paire, J.F. Guillemoles, L. Lombez, Contactless characterization of metastable defects in Cu(In, Ga)Se2 solar cells using time-resolved photoluminescence, Sol. Energy Mater. Sol. Cells **145**, 462 (2016)
9. S.D. Stranks, V.M. Burlakov, T. Leijtens, J.M. Ball, A. Goriely, H.J. Snaith, Recombination kinetics in organic-inorganic perovskites: excitons, free charge, and subgap states, Phys. Rev. Appl. **2**, 034007 (2014)
10. F. Staub, H. Hempel, J.-C. Hebig, J. Mock, U.W. Paetzold, U. Rau, T. Unold, T. Kirchartz, Beyond bulk lifetimes: insights into lead halide perovskite films from time-resolved photoluminescence, Phys. Rev. Appl. **6**, 044017 (2016)
11. M.J. Trimpl, A.D. Wright, K. Schutt, L.R.V. Buizza, Z. Wang, M.B. Johnston, H.J. Snaith, P. Muller-Buschbaum, L. M. Herz, Charge-carrier trapping and radiative recombination in metal halide perovskite semiconductors, Adv. Funct. Mater. **30**, 2004312 (2020)
12. L. Krückemeier, B. Krogmeier, Z. Liu, U. Rau, T. Kirchartz, Understanding transient photoluminescence in halide perovskite layer stacks and solar cells, Adv. Energy Mater. **11**, 2003489 (2021)
13. R. Brüggemann, S. Reynolds, Modulated photoluminescence studies for lifetime determination in amorphous-silicon passivated crystalline-silicon wafers, J. Non-Cryst. Solids **352**, 1888 (2006)
14. R. Bruggemann, M. Xu, J. Alvarez, M. Boutchich, J.-P. Kleider, Radiative recombination coefficient in crystalline silicon at low temperatures < 77 K by combined photoluminescence measurements, Energy Proc. **124**, 10 (2017)
15. J. Giesecke, *Quantitative Recombination and Transport Properties in Silicon from Dynamic Luminescence*, Springer Theses (Springer International Publishing, Cham, 2014)
16. D. Donetsky, S.P. Svensson, L.E. Vorobjev, G. Belenky, Carrier lifetime measurements in short-period InAs/GaSb strained-layer superlattice structures, Appl. Phys. Lett. **95**, 212104 (2009)
17. I. Reklaitis, R. Kudzma, S. Miasojedovas, P. Vitta, A. Zukauskas, R. Tomasiunas, I. Pietzonka, M. Strassburg, Photoluminescence decay dynamics in blue and green InGaN LED structures revealed by the frequency-domain technique, J. Electr. Mater. **45**, 3290 (2016)
18. J. Mickevicius, G. Tamulaitis, P. Vitta, A. Zukauskas, M.S. Shur, J. Zhang, J. Yang, R. Gaska, Carrier dynamics in GaN at extremely low excited carrier densities, Solid State Commun. **145**, 312 (2008)
19. M. Pawlak, K. Strzalkowski, Identification of the photoluminescence response in the frequency domain modulated infrared radiometry signal of ZnTe:Cr bulk crystal, Infrared Phys. Technol. **78**, 190 (2016)
20. Q. Sun, A. Melnikov, A. Mandelis, Y. Song, Fully nonlinear photocarrier radiometry / modulated photoluminescence dynamics in semiconductors: theory and applications to quantitative deconvolution of multiplexed photocarrier density wave interference and recombination processes, J. Luminescence **236**, 118075 (2021)
21. A. Melnikov, A. Mandelis, A. Soral, C. Zavala-Lugo, M. Pawlak, Quantitative imaging of defect distributions in CdZnTe wafers using combined deep-level photothermal spectroscopy, photocarrier radiometry, and lock-in carrierography, ACS Appl. Electr. Mater. **3**, 2551 (2021)
22. M. Orgeret, J. Boucher, Caracterisation d'un substrat semiconducteur par technique micro-onde et injection photonique, Rev. Phys. Appl. **13**, 29 (1978)
23. T. Otaredian, Analysis of microwave scattering from semiconductor wafers, Solid-State Electr. **36**, 163 (1993)
24. O. Palais, L. Clerc, A. Arcari, M. Stemmer, S. Martinuzzi, Mapping of minority carrier lifetime and mobility in imperfect silicon wafers, Mater. Sci. Eng. B **102**, 184 (2003)
25. I. Reklaitis, F. Nippert, R. Kudžma, T. Malinauskas, S. Karpov, I. Pietzonka, H.J. Lugauer, M. Strassburg, P. Vitta, R. TomašiūnasTomasiunas, A. Hoffmann, Differential carrier lifetime in InGaN-based light-emitting diodes obtained by small-signal frequency-domain measurements, J. Appl. Phys. **121**, 035701 (2017)
26. W. Zhao, B. Bérenguier, C. Rakotoarimanana, A. Goncalves, A. Etcheberry, M. Fregnaux, L. Lombez, J.-F. Guillemoles, Coupled time resolved and high frequency modulated photoluminescence probing surface passivation of highly doped n-type InP samples, J. Appl. Phys. **129**, 215305 (2021)
27. N. Moron, Modelisation analytique et simulation numerique de la technique de photoluminescence modulee appliquee a des materiaux semi-conducteurs, Ph.D. thesis, Université Paris-Saclay, 2021
28. N. Moron, B. Berenguier, J. Alvarez, J.-P. Kleider, Analytical model of the modulated photoluminescence in semiconductor materials, J. Phys. D: Appl. Phys. **55**, 105103 (2022)
29. M. Maiberg, T. Holscher, S. Zahedi-Azad, R. Scheer, Theoretical study of time-resolved luminescence in semiconductors. III. Trap states in the band gap, J. Appl. Phys. **118**, 105701 (2015)

Cite this article as: Baptiste Bérenguier, Alban Asseko, Hiba Haddara, Sylvain Le Gall, Jean-Paul Kleider, Jean-François Guillemoles, Contactless defects detection using modulated photoluminescence technique: model for a single Shockley-Read-Hall trap in a semiconductor thin layer, EPJ Photovoltaics **16**, 11 (2025)